



Tailoring the crystal forms of the Ni-MOF catalysts for enhanced photocatalytic CO₂-to-CO performance

Kainan Song^a, Shujie Liang^a, Xiaohui Zhong^a, Mengye Wang^{c,d}, Xiaofeng Mo^a, Xueqian Lei^{a,*}, Zhang Lin^{a,b}

^a School of Environment and Energy, Guangdong Provincial Key Laboratory of Solid Wastes Pollution Control and Recycling, South China University of Technology, Guangzhou, Guangdong 510006, PR China

^b Chinese National Engineering Research Center for Control & Treatment of Heavy Metal Pollution, School of Metallurgy and Environment, Central South University, Changsha, Hunan 410083, PR China

^c School of Materials, Sun Yat-Sen University, Shenzhen 518107, PR China

^d State Key Laboratory of Optoelectronic Materials and Technologies, Sun Yat-Sen University, Guangzhou 510275, China

ARTICLE INFO

Keywords:

Ni-MOF
Crystal forms
Nanocatalysts
Photocatalytic CO₂ reduction

ABSTRACT

While semiconductor nanocrystals with different crystal forms typically show different catalytic performances, such behavior has been scarcely documented for metal-organic frameworks (MOFs). Herein, two Ni-MOF catalysts with different crystal forms have been successfully prepared and used in photo-reduction of CO₂. With a prolonged lifetime (5 h vs 2 h) and higher yield of the product CO (34 μmol vs 18 μmol), Ni-MOF(H₂O) demonstrates a much better performance than Ni-MOF. Theoretical studies reveal that the adsorption energy of a CO₂ molecule is more negative on Ni-MOF(H₂O) than on Ni-MOF (−0.85 eV vs −0.62 eV). Furthermore, the transfer and separation of the photo-generated charge carriers are also more efficient in the Ni-MOF(H₂O) system. This study not only presents a superior Ni-MOF catalyst but also promotes the fabrication of highly active catalysts for the photo-reduction of CO₂.

1. Introduction

The photo-reduction of CO₂ yielding valuable fuels or chemical feedstocks has gained considerable attention as a promising strategy to simultaneously alleviate the global warming and produce green energy or green chemicals [1,2]. However, the efficiency of photocatalytic CO₂ conversions is still relatively low because of the thermodynamic and kinetic stability of CO₂; furthermore, its reaction mechanism is still poorly understood at present [3,4]. This low efficiency needs to be addressed by the design and construction of high-performance catalysts [5–8]. As previously reported, catalysts with different crystal forms would exhibit greatly different catalytic properties [9,10]. For instance, TiO₂ in its anatase form usually displays better photocatalytic performances than rutile TiO₂ and brookite TiO₂ [11–13] due to the longer lifetime of photo-generated charges and the lighter effective mass of photo-induced electrons and holes in anatase TiO₂ [14]. However, Junie et al [15], found that the existence of an appropriate depth of the photo-generated electron trap in brookite TiO₂ can significantly contribute to improve its overall photocatalytic performance. As the

deepening understanding of the structural properties of TiO₂ with different crystal forms, the performance of TiO₂ nanocatalyst is constantly improved.

Metal-organic frameworks (MOFs) catalysts have been increasingly used in the photo-reduction of CO₂ because of their advantageous properties, including strong adsorption abilities for gas molecules, adjustable structures, and unique photo-electrochemical properties [16, 17]. Similar to semiconductor catalysts, the crystal forms or morphologies of MOFs catalysts have a significant impact on their catalytic performances [9,18]. Recently, Wang et al [19], successfully synthesized three ZIF-67 catalysts with different crystal forms and morphologies via a solvothermal process. For the photo-reduction of CO₂, the ZIF-67 with a leaf-like morphology showed the highest photocatalytic activity. Thus, investigating the relationship between catalytic activity for CO₂ photo-reduction and the crystal form of MOFs catalysts could provide deep insight for the design of improved catalysts. However, only a few related studies have been conducted, and the topic has not yet been researched in depth.

Ni-MOFs have been used as the catalyst in the photocatalytic CO₂-to-

* Corresponding author.

E-mail address: xqlei@scut.edu.cn (X. Lei).

<https://doi.org/10.1016/j.apcatb.2022.121232>

Received 30 November 2021; Received in revised form 14 February 2022; Accepted 19 February 2022

Available online 22 February 2022

0926-3373/© 2022 Elsevier B.V. All rights reserved.

CO reaction, and exhibited better performance than their isostructural MOF catalysts (Co-MOF, Cu-MOF, Fe-MOF, and other) [20,21]. While several related studies reported complicated synthesis processes of Ni-MOF, including the use of trimethylamine [22], the need of prolonged ultrasonic treatment [23], and the assistance of unfocused infrared laser [24], such materials could be conveniently obtained via the direct reaction between Ni(OH)₂ and organic linkers [25,26]. Two-dimensional (2D) Ni-MOF nanosheets were usually acquired as the final products by the above-mentioned method, and the thicknesses of the nanosheets could be regulated by changing the volume ratio of the N, N-dimethylformamide (DMF) and H₂O [27,28]. According to the growth law of MOFs crystals [8,29], it is possible to fabricate Ni-MOF catalysts with different crystal forms by adjusting the reaction parameters.

Therefore, the relationship between different crystal forms of Ni-MOF synthesized via a facile process and their photocatalytic activities for CO₂ reduction should be investigated. The research results would not only provide guidance for the design of high-performance catalysts for the photo-reduction of CO₂ but also promote the large-scale production of MOFs catalysts.

2. Experimental

2.1. Synthesis of bulk Ni(OH)₂

NiCl₂·6H₂O (6 mmol) was dissolved in 54 mL H₂O under stirring at room temperature. A NaOH solution (2 M, 6 mL) was added dropwise (0.5 mL/min) to the solution. The obtained mixture was transferred into a 100 mL Teflon-lined stainless-steel autoclave and heated at 180 °C for 12 h. After cooling to room temperature, the precipitate was collected by centrifugation, washed three times with H₂O and EtOH, and dried by vacuum freeze-drying.

2.2. Synthesis of Ni-MOF(H₂O)

Bulk Ni(OH)₂ (0.047 g, 0.51 mmol) and terephthalic acid (BDC) (0.085 g, 0.51 mmol) were added to 40 mL of DMF-H₂O mixtures [v (DMF): v(H₂O) = 1: 1]. After ultrasonic treatment for 5 min, the mixture, placed in a flask equipped with a reflux condenser, was heated in an oil bath at 90 °C for 6 h under stirring at a speed of 500 rpm. Finally, the resulting products were collected by centrifugation at 9000 rpm for 3 min, washed three times with H₂O and DMF, and dried in a vacuum oven at 50 °C overnight.

As listed in Table 1, different Ni-MOF materials could be prepared by changing the synthesis parameters (DMF/H₂O ratio, heating temperature). Ni-MOF(H₂O) was also prepared via a green route, using the original electro-plating sludge (EPS) and waste PET plastic derived BDC instead of bulk Ni(OH)₂ and commercial BDC, respectively.

2.3. Photocatalytic CO₂ reduction

Typically, 7.5 mg photosensitizer [Ru(2,2'-bipyridyl)₃]Cl₂·6 H₂O (abbreviated as Ru), 1.0 mg catalyst, 3 mL acetonitrile (MeCN), 2 mL H₂O and 1 mL triethanolamine (TEOA) as sacrificial reducing agent were added into the quartz reactor. The light source was a 5 W white

LED lamp (400–1000 nm, PCX50A Discover, Beijing Perfect Light Technology). Before light irradiation, the quartz bottle was evacuated and backfilled with high-purity CO₂ to reach a pressure of 1 atm. The reaction system was continuously stirred during the photoreduction process. Gas samples were taken at specific times during the photoreaction and analyzed by an Agilent 7890B gas chromatography system equipped with a flame ionization detector and thermal conductivity detector. To evaluate its reusability, 50 mg of the Ni-MOF(H₂O) was applied as catalyst in the photoreduction of CO₂ and recovered by centrifugation after each run. After washing and drying, the used catalyst was recycled by combining with fresh 7.5 mg Ru, 3 mL MeCN, 2 mL H₂O and 1 mL TEOA for the next run.

Selectivity for CO was calculated according to the equation below, in which R (CO) and R(H₂) refer to the formation rates of the gas products CO and H₂ in μmol/h, respectively.

$$\text{Selectivity of CO} = \frac{R(\text{CO})}{R(\text{CO}) + R(\text{H}_2)} \times 100\%$$

The apparent quantum yield (AQY) was determined under the same photo-reduction conditions using radiation of monochromatic light at 420 nm. The illumination intensity was measured using an USR-40 spectroradiometer (Ushio Inc., Japan), and AQY was calculated using the equation below:

$$\text{AQY}(\%) = 100\% \times \frac{\text{number of consumed electrons}}{\text{number of incident electrons}} = 100\% \times \frac{\text{number of evolved (CO + H}_2\text{) molecules}}{\text{number of incident electrons}}$$

2.4. Materials characterization

Crystal forms of catalysts were analyzed by X-ray diffraction (XRD) on a Bruker D8 Advance X-ray diffractometer using Cu-Kα radiation. High resolution transmission electron microscopy (HR-TEM, JEM-2100 F), elemental mapping using energy-dispersive X-ray spectroscopy (EDX), and field emission scanning electron microscopy (FE-SEM, Hitachi Regulus 8100) were employed to determine the structure and elemental distribution of the catalysts. X-ray photoelectron spectroscopy (XPS) was performed on a Escalab 250Xi spectrometer, and the binding energies were referenced to the C1s peak at 284.6 eV. N₂ adsorption/desorption isotherms and CO₂ adsorption isotherms were recorded and analyzed using a Micromeritics ASAP 2020 system. Catalysts were degassed in vacuum at 120 °C for 6 h prior to measurement. Fourier transform infrared spectroscopy (FTIR) and Raman spectroscopy were conducted on a Nexus 670 FTIR spectrometer and a DXR 2xi Raman spectrometer, respectively. Thermogravimetry (TG) was performed on a Netzsch STA449C/4/G instrument. Time-resolved photoluminescence (PL) spectra and steady-state PL spectra of the photocatalytic reaction systems were recorded and analyzed on an FLS980 spectrometer (540 nm, room temperature). Electrochemical impedance spectroscopy (EIS) were performed on a CHI 660E electrochemical workstation using test parameters described in our previous work [30].

3. Results and discussions

3.1. Catalyst characterization

First, the bulk Ni(OH)₂ with a hexagonal plate-like morphology (Fig. S1) was synthesized by a simple hydrothermal process. Afterward, Ni-MOF catalysts with different crystal forms were obtained by the reaction of bulk Ni(OH)₂ and BDC in DMF-H₂O solvent (Fig. 1). Ni-MOF(H₂O) was synthesized in a 1:1 (v/v) DMF/H₂O mixture at 90 °C, while the Ni-MOF was obtained from a 9:1 (v/v) DMF-H₂O mixture at 140 °C.

The XRD patterns of Ni-MOF(H₂O) and Ni-MOF are different (Figs. 2 and S2). For Ni-MOF(H₂O), the diffraction peaks at 2θ values of 9.38°, 15.68°, 23.96°, 11.92°, and 29.22° are assigned to (100), (10–1), (020), (010) and (-1-21) crystal planes of [Ni₃(OH)₂(C₈H₄O₄)₂(H₂O)₄]·2H₂O (CCDC No. 638866), respectively [31,32]. In the structure of this

Table 1
Synthesis parameters of Ni-MOF samples with different crystal forms.

Sample	Ni (OH) ₂ (mmol)	BDC (mmol)	DMF (mL)	H ₂ O (mL)	Temp. (°C)	Time (h)
Ni-MOF (H ₂ O)	0.51	0.51	20	20	90	6
Samp. 2	0.51	0.51	20	20	120	12
Samp. 3	0.51	0.51	20	20	140	12
Ni-MOF	0.51	0.51	36	4	140	12

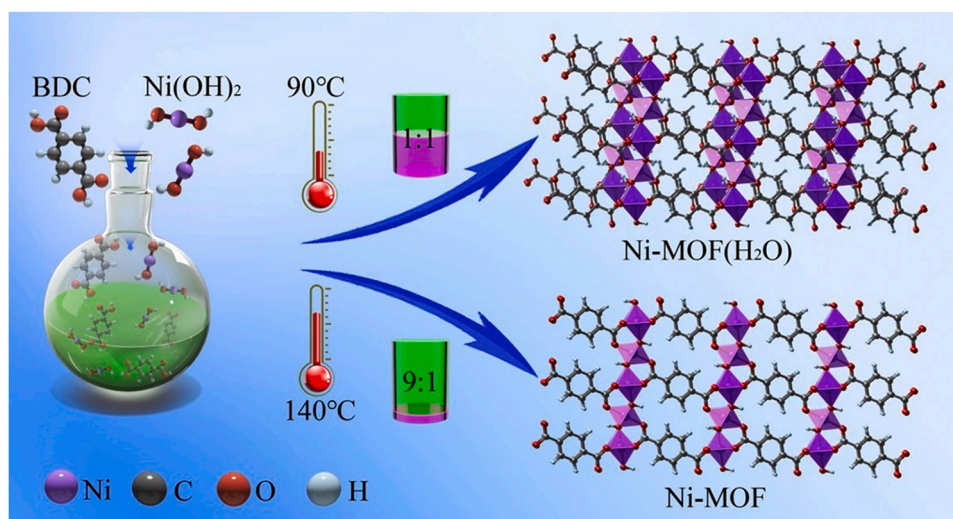


Fig. 1. Schematic illustration of the synthesis process of Ni-MOF(H₂O) and Ni-MOF.

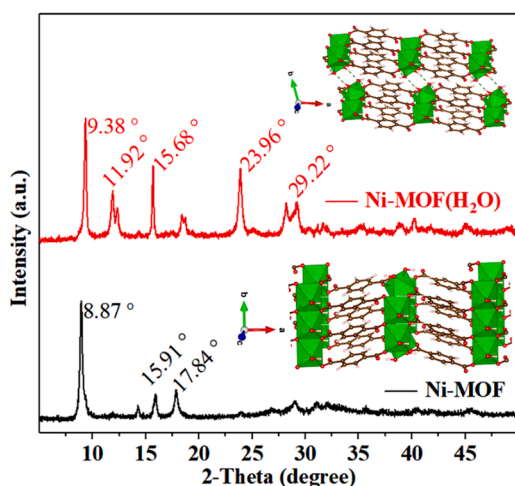


Fig. 2. XRD patterns of Ni-MOF(H₂O) and Ni-MOF. The insets are schematic diagrams of the crystal structures of the two catalysts.

compound [33–35], Ni atoms are present in two different coordination modes, linked to a group of six O atoms to form octahedrons. Ni(1) is coordinated by two –OH, two O atoms from organic linkers and two O atoms from H₂O molecules. Ni(2) is coordinated by four O atoms from organic linkers and two –OH. The reproduced crystal unit is the chain [Ni(1)O₆]₂[Ni(2)O₆], in which Ni(1) octahedrons are connected by edges sharing and linked to the vertex of Ni(2) octahedron via –OH. Two adjacent Ni chains are linked by BDC anions to form infinite sheets parallel to the (010) facets, and the interchain hydrogen bonds between structural H₂O molecules hold the 2D sheets together. For Ni-MOF, the strongest diffraction peak at $2\theta = 8.87^\circ$ is attributed to the (200) crystal facet of [Ni₂(OH)₂(C₈H₄O₄)] (CCDC No. 985792), and the diffraction peaks at 2θ of 15.91° and 17.84° are corresponding to (201) and (–201) planes, respectively [22]. Ni-MOF exhibits the same crystal structure as [Co₂(OH)₂(C₈H₄O₄)] [36,37], both of which belong to the monoclinic system. In the structure, two types of Ni atoms with different coordination environments exist. Both Ni(1) and Ni(2) atoms are six-coordinated to form octahedrons. Ni(1) is coordinated by four –OH and two O atoms from organic linkers, while the Ni(2) is connected to two –OH and four O atoms from organic linkers. These octahedrons are interconnected in the (100) crystallographic plane to form 2D Ni layers separated by randomly disordered BDC molecules, as shown in the

illustration (Fig. 2).

In the SEM and TEM images of as-obtained Ni-MOF (Fig. 3, a and b), the catalyst displays a morphology of flexible nanosheets with irregular shapes. Ni-MOF(H₂O), however, exhibits rhombus-shaped plates with lengths ranging from several hundred nanometers to 1.5 micrometers (Fig. 3, c and d). Elemental mapping of these plates (Fig. 3e) demonstrates a uniform distribution of C, O and Ni elements throughout the entire Ni-MOF(H₂O) surfaces. Quantitative EDX measurements reveal that this compound contains 36.0 wt% Ni, 33.6 wt% O and 30.4 wt% C (Fig. 3f), which is close to the reported value [35].

TG measurements were conducted between 25 °C and 1000 °C in air with a heating rate of 5 °C/min to determine the difference of the catalysts in thermal stability and estimate their Ni content. The slight weight loss up to 350 °C (Fig. S3a) is attributed to the loss of H₂O molecules absorbed on the Ni-MOF surface. The rapid and substantial weight loss between 350 °C and 400 °C is caused by the conversion of [Ni₂(OH)₂(C₈H₄O₄)] to NiO [36]. A significant difference is observed between the TG curves of Ni-MOF(H₂O) and Ni-MOF. About 10 wt% weight loss between 200 °C and 370 °C could be attributed to the loss of structural H₂O molecules in Ni-MOF(H₂O) [35]. Based on the residual weight, the content of Ni in Ni-MOF(H₂O) and Ni-MOF was calculated as 31.0 wt% and 35.6 wt%, respectively. Ni-MOF exhibits a BET surface area of 81.5 m²/g (Fig. S3b), which is about 3.5 times larger than that of Ni-MOF(H₂O). The Raman spectra of the two compounds are very similar (Fig. S3c). The intensity of the peak at 1561 cm^{–1}, which is attributed to the symmetrical stretching vibration of C–O in the COO-group [38–40], is higher for Ni-MOF than for Ni-MOF(H₂O). The baseline in the spectrum of Ni-MOF is slanted, which might be caused by fluorescence interference [41]. In the FTIR spectra (Fig. S3d), Ni-MOF(H₂O) and Ni-MOF show the same intense IR bands at around 1580 cm^{–1} and 1365 cm^{–1}, which correspond to the asymmetrical and symmetrical stretching vibration of –COO– group, respectively [39,40]. The two bands at 3426 cm^{–1} and 3066 cm^{–1} imply the presence of structural H₂O molecules in the Ni-MOF(H₂O) [37]. For Ni-MOF, there is a weak band at around 3318 cm^{–1}, which is assigned to the characteristic band of H₂O molecules absorbed on its surface [36]. These results are in accordance with those of Raman, TG and XRD measurements.

XPS spectra of Ni-MOF(H₂O) and Ni-MOF are shown in Fig. S4. For both catalysts, only peaks corresponding to the C, O and Ni elements could be found in the survey spectra. Fitting results of the Ni 2p spectra indicate that the valence state of Ni in the two samples is + 2 [22,42]. Carbon groups such as C=C and O=C=O can be differentiated in the C 1s peaks of the two catalysts [34,39,43,44]. The peak of the O=C=O group of Ni-MOF(H₂O), moves towards smaller binding energy

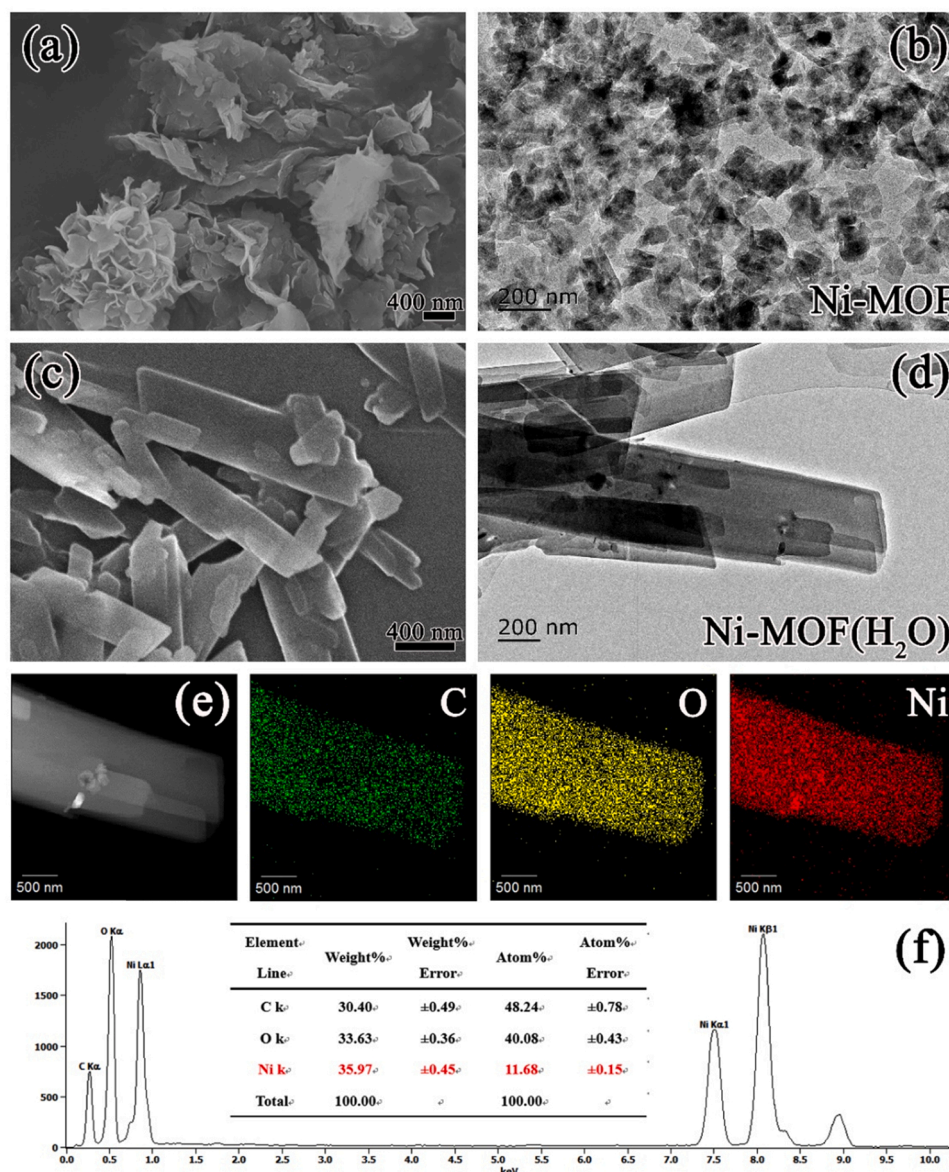


Fig. 3. SEM and TEM images of the Ni-MOF (a, b) and Ni-MOF(H₂O) (c, d). TEM mapping image (e) and EDX spectrum (f) of Ni-MOF(H₂O).

(Fig. S4c), comparing with that of Ni-MOF. Furthermore, there is an obvious difference between the O 1s spectrum of the two samples. Although the O elements both exist in the forms of C-O and O-H [38,40], the proportion of O-H in Ni-MOF is 14.7%, while that of Ni-MOF(H₂O) is 29.2%. Considering the differences in crystal phase, morphology, Ni content, BET surface area, and functional group between Ni-MOF(H₂O) and Ni-MOF, the photocatalytic performance of the two catalysts should be different.

3.2. Photocatalytic activities of the catalysts

The photocatalytic activities of Ni-MOF(H₂O) and Ni-MOF for CO₂ reduction were explored under visible-light irradiation. Using the Ru compound as photosensitizer and TEOA as sacrificial agent [41–43], the reactions were conducted in a quartz reactor containing a CO₂-saturated CH₃CN-H₂O mixture [45–47].

First, the effect of the dosage of Ni-MOF(H₂O) catalyst on the formation rate of CO and H₂ was explored. An amount of 1.0 mg Ni-MOF(H₂O) gives the highest CO formation rate of ca. 9.5 mmol/h/g under otherwise equal conditions (Fig. 4a), suggesting that more photo-

electrons generated from Ru could have been shifted to the Ni²⁺ active sites [24,48]. Therefore, a catalyst amount of 1.0 mg was used in the following experiments (except for the cycling test). Fig. 4b shows the photocatalytic activities of the four synthesized Ni-organic catalysts during a 2-hour irradiation period. The Ni-MOF(H₂O) catalyst shows the best performance with CO and H₂ formation rates of 9.61 mmol/h/g and 0.48 mmol/h/g, respectively, and a selectivity to CO of 95.24%. The catalysts Samp. 2 and Samp. 3 show almost the same photocatalytic activity as Ni-MOF(H₂O), which can be attributed to their identical crystal forms and morphologies (Table 1, Figs. S5 and S6). However, Ni-MOF shows relatively poor activity, affording a CO production rate of 8.1 mmol/h/g. AQY for CO generation by Ni-MOF(H₂O) reached 1.28% ($\lambda = 420$ nm), which is quite superior to similar systems (Table S1). Furthermore, CO and H₂ are the only gas products (Fig. S7), and no liquid products such as HCOOH and CH₃OH have been detected (Fig. S8).

The formations of CO and H₂ from Ni-MOF(H₂O) and Ni-MOF photocatalytic systems are shown in Fig. 4c as functions of irradiation time. As expected, Ni-MOF(H₂O) exhibits much better performance, and the CO yield of about 34 μ mol after 6 h is 1.8 times higher than that of Ni-

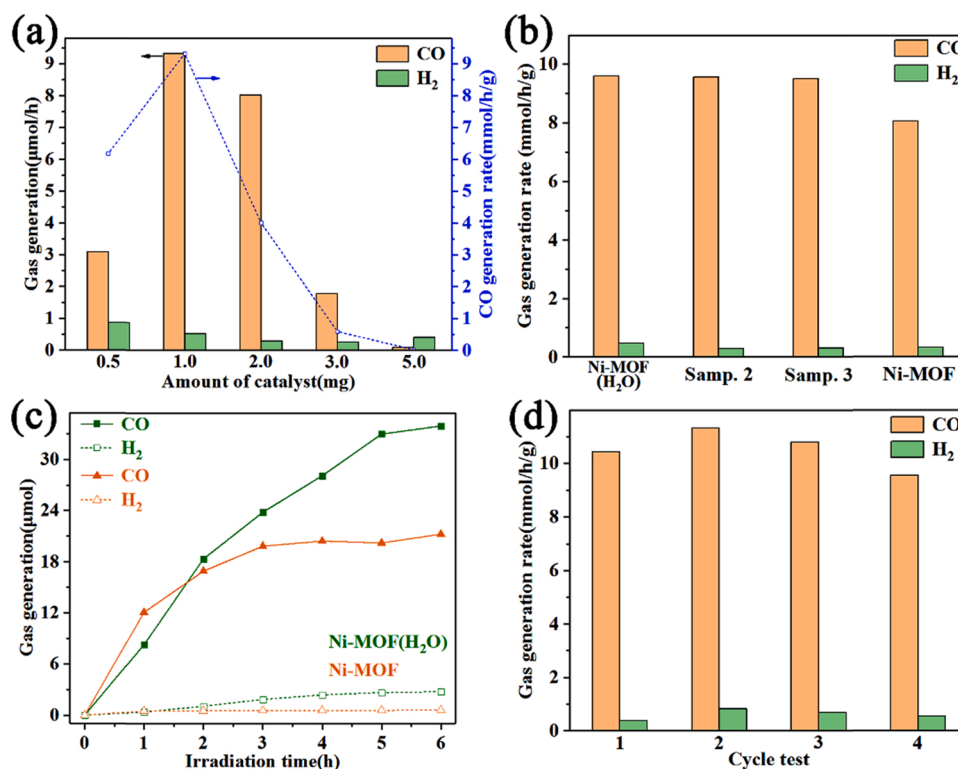


Fig. 4. (a) Effect of Ni-MOF(H₂O) dosage on the formation rate of CO and H₂. (b) Photocatalytic performances of different Ni-MOF catalysts. (c) Yields of CO and H₂ as functions of irradiation time. (d) Cycle test of the Ni-MOF(H₂O) catalyst.

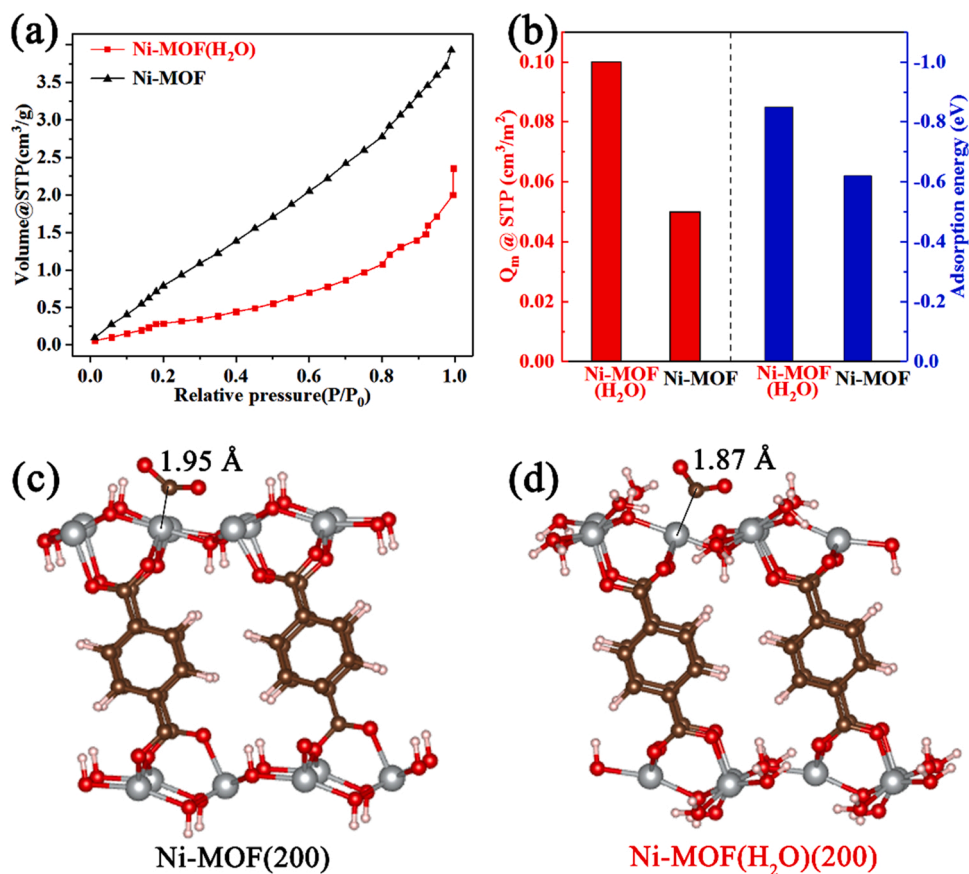


Fig. 5. CO₂ adsorption isotherms (a), comparison of the adsorption capacities for CO₂ molecules (b), and DFT calculation results of CO₂ molecule adsorption on a Ni site of (200) planes in Ni-MOF (c) and Ni-MOF(H₂O) (d).

MOF. Furthermore, Ni-MOF(H₂O) could maintain its catalytic activity for at least 5 h, which is much longer than observed for Ni-MOF. In addition, catalyst recyclability of Ni-MOF(H₂O) after reaction times of 2 h was tested. CO and H₂ yields in each cycle remain almost unchanged (Fig. 4d), demonstrating the good recyclability of the Ni-MOF(H₂O) catalyst. No obvious crystal phase and morphology changes were observed after four consecutive cycles (Figs. S9 and S10), suggesting excellent structural stability of the catalyst. Using a Ni-containing electroplating sludge and BDC derived from waste PET plastic instead of the bulk Ni(OH)₂ and commercial BDC, Ni-MOF(H₂O) with rhombus-plate morphology could also be fabricated (Fig. S11). This material also exhibits much better photocatalytic performance (CO formation rate of ca. 10 mmol/h/g) than the Ni-MOF synthesized from purchased chemical reagents (CO formation rate of less than 8 mmol/h/g) (Fig. S12).

To elucidate the excellent CO₂ photo-reduction performance of Ni-MOF(H₂O), a series of photo-electrochemical characterizations was performed. As shown in Fig. 5a, under normal pressure, the CO₂ adsorption capacity of Ni-MOF is much higher than that of Ni-MOF(H₂O) (3.93 vs 2.35 cm³/g). However, the CO₂ adsorption capacity per unit specific surface area is about two times higher for Ni-MOF(H₂O) than for Ni-MOF (Fig. 5b, red columns). The result is in agreement with the DFT calculation results. The adsorption energy of CO₂ molecule on Ni-MOF(H₂O) is −0.85 eV (Fig. 5b, blue columns), which absolute value is higher than that of Ni-MOF (−0.62 eV). In addition, the length of the Ni-C bond of 1.87 Å in Ni-MOF(H₂O) (Fig. 5d) is much shorter than that in Ni-MOF (1.95 Å). Thus, the CO₂ adsorption performance [20,49] of Ni-MOF(H₂O) is considerably better than that of Ni-MOF.

In the EIS investigations, a much smaller semicircle is observed in the Nyquist plot of Ni-MOF(H₂O) than in that of Ni-MOF (Fig. 6a and b), implying a much lower charge-transfer resistance in the Ni-MOF(H₂O) catalyst, which promotes the fast transport of photo-generated carriers [30,50]. In Fig. 6c, the Ni-MOF systems show enhanced PL intensities compared to the catalyst-free system, indicating the radiative

recombination of photo-generated carriers and enhanced separation efficiency of photo-induced electrons and holes [51,52] in the Ni-MOF systems. Furthermore, the PL lifetime (Fig. 6d) of Ni-MOF(H₂O) (286.9 ns) is shorter than that of Ni-MOF (298.0 ns), indicating more effective separation of photo-induced charge carriers [53,54] in the former system. All these results suggest that the Ni-MOF(H₂O) system exhibits stronger adsorption capacity for CO₂ molecules, lower resistance for the transfer of photo-generated charge carriers, and more efficient separation of electrons and holes than the Ni-MOF system, thus displaying excellent performance for CO₂ photo-reduction.

A series of control experiments were conducted to explore the possible mechanism of the photo-reduction reaction. In the catalyst-free reaction system, the production of CO (0.38 μmol/h) and CO selectivity (43.68%) decreased dramatically compared to the Ni-MOF(H₂O)-containing system (Fig. S13a, column 2), indicating the main function of the catalyst in the transformation reaction from CO₂ to CO [49,55]. When performing the reaction in an Ar atmosphere, CO could not be detected in the reaction system (Fig. S13a, column 3), suggesting that the product CO stems from the feedstock CO₂ [23,24]. The result of the labeling experiment using ¹³CO₂ gas (Fig. S14), also demonstrates the source of the reaction. CO formation is not observed in the absence of Ru or light irradiation (Fig. S13a, column 4 and column 5), implying that the CO₂ reduction reaction is initiated by photocatalysis [48,56]. Furthermore, the sacrificial agent (TEOA) was also found to be necessary for the photo-reduction of CO₂ to CO (Fig. S13a, column 6). As shown in Fig. S13b, the trend of CO generation matches well with the optical absorption of Ru, suggesting that the CO₂ reduction reaction to CO is triggered by the photoexcitation of Ru [23,56].

Based on the abovementioned results, a possible mechanism for the photoreduction of CO₂ on the Ni-MOF-based catalyst systems has been proposed (Fig. 7). Upon visible-light irradiation, Ru is excited and then quenched by the sacrificial agent (TEOA) to form a reduced species of Ru. Subsequently, the reduced photosensitizers could transfer electrons

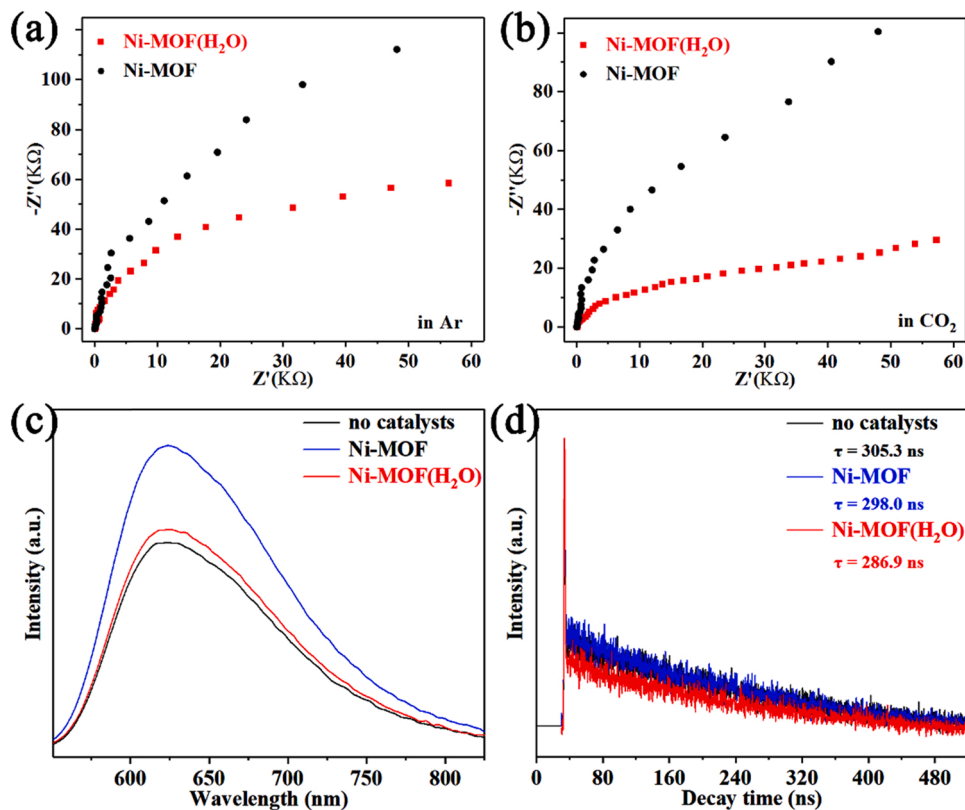


Fig. 6. (a) EIS curves in Ar atmosphere, (b) EIS curves in CO₂ atmosphere, (c) steady-state PL spectra and (d) time-resolved transient PL decay spectra of Ni-MOF(H₂O) and Ni-MOF.

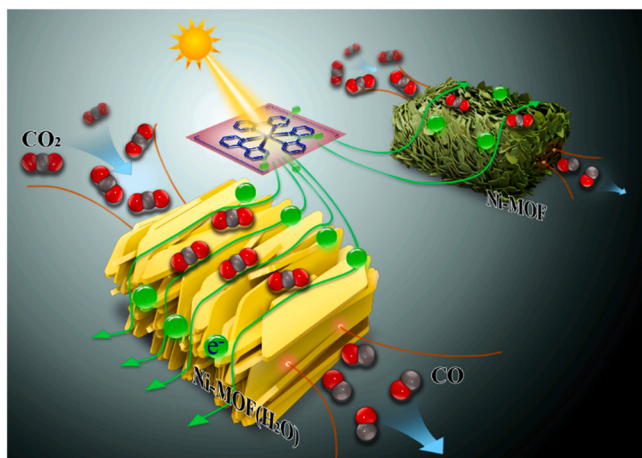


Fig. 7. Proposed mechanism of CO₂ photo-reduction based on Ni-MOFs catalyst.

to Ni-MOF catalyst. Finally, the electrons transfer to the active Ni sites where CO₂ molecules are adsorbed and then participate in the transformation of CO₂ to CO. Furthermore, a small number of protons present in the system could also be reduced by the photo-generated electrons to yield the byproduct H₂.

4. Conclusions

In summary, two Ni-based MOFs with different composition and crystal forms were successfully synthesized via the reaction of bulk Ni(OH)₂ and BDC in DMF-H₂O solvents. Ni-MOF(H₂O) exhibits thicker plate morphology, lower Ni content, and a much smaller BET surface areas than Ni-MOF. For the photocatalytic reduction of CO₂, however, the CO yield from the Ni-MOF(H₂O) catalyst is 1.8 times higher than that of the Ni-MOF catalyst under otherwise identical conditions. DFT calculation and several photo-electrochemical characterization results suggest that the Ni-MOF(H₂O) system exhibits stronger adsorption ability for CO₂ molecules, lower charge transfer resistance, and a lower recombination rate of photo-generated charge carriers than the Ni-MOF system, thus displaying superior activity for the photoreduction of CO₂. This study represents the first example of improving catalytic performance by tailoring the crystal forms of Ni-MOF, and our findings could promote the design of efficient MOF catalysts for photocatalytic applications.

CRediT authorship contribution statement

Kainan Song: Investigation, Formal analysis, Validation, Writing-original draft, Writing-review & editing. **Shujie Liang:** Formal analysis, Conceptualization, Writing-review & editing. **Xiaohui Zhong:** Formal analysis, Writing-review & editing. **Mengye Wang:** synchrotron powder diffraction measurement, the labeling experiment using ¹³CO₂ gas. **Xiaofeng Mo:** DFT calculations, Conceptualization. **Xueqian Lei:** Conceptualization, Formal analysis, Writing-review & editing, Funding acquisition. **Zhang Lin:** Resources, Project administration, Supervision.

Declaration of Competing Interest

The authors declare that they have no known competing financial interests or personal relationships that could have appeared to influence the work reported in this paper.

Acknowledgements

This research was financially supported by the National Key

Research and Development Program of China (No. 2019YFA0210400), National Natural Science Foundation of China (Grant No. 21836002 and 52100144), Guangdong Science and Technology Program (No. 2020B121201003) and Guangdong Basic and Applied Basic Research Foundation (2021A1515010356).

Appendix A. Supporting information

Supplementary data associated with this article can be found in the online version at doi:10.1016/j.apcatb.2022.121232.

References

- [1] Y. Zhang, B. Xia, J. Ran, K. Davey, S.Z. Qiao, Atomic-level reactive sites for semiconductor-based photocatalytic CO₂ reduction, *Adv. Energy Mater.* 10 (2020) 1903879–1903901.
- [2] X. Li, J. Yu, M. Jaroniec, X. Chen, Cocatalysts for selective photoreduction of CO₂ into solar fuels, *Chem. Rev.* 119 (2019) 3962–4179.
- [3] W.A. Thompson, E. Sanchez Fernandez, M.M. Maroto-Valer, Review and analysis of CO₂ photoreduction kinetics, *ACS Sustain. Chem. Eng.* 8 (2020) 4677–4692.
- [4] P. Liu, X. Peng, Y.-L. Men, Y.-X. Pan, Recent progresses on improving CO₂ adsorption and proton production for enhancing efficiency of photocatalytic CO₂ reduction by H₂O, *Green Chem. Eng.* 1 (2020) 33–39.
- [5] Z. Zhang, G. Yi, P. Li, X. Zhang, H. Fan, X. Wang, C. Zhang, Y. Zhang, Engineering approach toward catalyst design for solar photocatalytic CO₂ reduction: a critical review, *Int. J. Energy Res.* 45 (2021) 9895–9913.
- [6] R.R. Ikreedeegh, M. Tahir, A critical review in recent developments of metal-organic-frameworks (MOFs) with band engineering alteration for photocatalytic CO₂ reduction to solar fuels, *J. CO₂ Util.* 43 (2021) 101381–101421.
- [7] S. Wang, X. Han, Y. Zhang, N. Tian, T. Ma, H. Huang, Inside-and-out semiconductor engineering for CO₂ photoreduction: from recent advances to new trends, *Small Struct.* 2 (2020) 2000061–2000109.
- [8] Q. Wang, D. Astruc, State of the art and prospects in metal-organic framework (MOF)-based and MOF-derived nanocatalysis, *Chem. Rev.* 120 (2020) 1438–1511.
- [9] H. Chang, Y. Zhou, S. Zhang, X. Zheng, Q. Xu, CO₂-induced 2D Ni-BDC metal-organic frameworks with enhanced photocatalytic CO₂ reduction activity, *Adv. Mater. Int.* 8 (2021) 2100205–2100211.
- [10] R. Kaplan, B. Erjavec, G. Dražić, J. Grdadolnik, A. Pintar, Simple synthesis of anatase/rutile/brookite TiO₂ nanocomposite with superior mineralization potential for photocatalytic degradation of water pollutants, *Appl. Catal. B* 181 (2016) 465–474.
- [11] L. Liu, H. Zhao, J.M. Andino, Y. Li, Nanoparticulate X-ray computed tomography contrast agents: from design validation to in vivo applications, *ACS Catal.* 2 (2012) 1817–1828.
- [12] W. Kim, T. Tachikawa, Gh Moon, T. Majima, W.J.A.C. Choi, Molecular-level understanding of the photocatalytic activity difference between anatase and rutile nanoparticles, *Angew. Chem. Int. Ed.* 126 (2014) 14260–14265.
- [13] T. Luttrell, S. Halpegamage, J. Tao, A. Kramer, E. Sutter, M. Batzill, Why is anatase a better photocatalyst than rutile?—Model studies on epitaxial TiO₂ films, *Sci. Rep.* 4 (2014) 4043–4050.
- [14] J. Zhang, P. Zhou, J. Liu, J. Yu, New understanding of the difference of photocatalytic activity among anatase, rutile and brookite TiO₂, *Phys. Chem. Chem. Phys.* 16 (2014) 20382–20386.
- [15] J.J.M. Vequizo, H. Matsunaga, T. Ishiku, S. Kamimura, T. Ohno, A. Yamakata, Trapping-induced enhancement of photocatalytic activity on brookite TiO₂ powders: comparison with anatase and rutile TiO₂ powders, *ACS Catal.* 7 (2017) 2644–2651.
- [16] Y. Qian, F. Zhang, H. Pang, A review of MOFs and their composites-based photocatalysts: synthesis and applications, *Adv. Funct. Mater.* 31 (2021) 2104231–2104264.
- [17] D. Li, M. Kassymova, X. Cai, S.-Q. Zang, H.-L. Jiang, Photocatalytic CO₂ reduction over metal-organic framework-based materials, *Coord. Chem. Rev.* 412 (2020) 213262–213277.
- [18] W. Yang, H.J. Wang, R.R. Liu, J.W. Wang, C. Zhang, C. Li, D.C. Zhong, T.B. Lu, Tailoring crystal facets of metal-organic layers to enhance photocatalytic activity for CO₂ reduction, *Angew. Chem. Int. Ed.* 60 (2021) 409–414.
- [19] M. Wang, J. Liu, C. Guo, X. Gao, C. Gong, Y. Wang, B. Liu, X. Li, G.G. Gurzadyan, L. Sun, Metal-organic frameworks (ZIF-67) as efficient cocatalysts for photocatalytic reduction of CO₂: the role of the morphology effect, *J. Mater. Chem. A* 6 (2018) 4768–4775.
- [20] B. Han, X. Ou, Z. Zhong, S. Liang, X. Yan, H. Deng, Z. Lin, Photoconversion of anthropogenic CO₂ into tunable syngas over industrial wastes derived metal-organic frameworks, *Appl. Catal. B* 283 (2021) 119594–119601.
- [21] Z. Wang, J. Fan, B. Cheng, J. Yu, J. Xu, Nickel-based cocatalysts for photocatalysis: Hydrogen evolution, overall water splitting and CO₂ reduction, *Mater. Today Phys.* 15 (2020) 100279–100305.
- [22] S. Zhao, Y. Wang, J. Dong, C.-T. He, H. Yin, P. An, K. Zhao, X. Zhang, C. Gao, L. Zhang, J. Lv, J. Wang, J. Zhang, A.M. Khattak, N.A. Khan, Z. Wei, J. Zhang, S. Liu, H. Zhao, Z. Tang, Ultrathin metal-organic framework nanosheets for electrocatalytic oxygen evolution, *Nat. Energy* 1 (2016) 1–10.

- [23] B. Han, X. Ou, Z. Deng, Y. Song, C. Tian, H. Deng, Y.J. Xu, Z. Lin, Nickel metal-organic framework monolayers for photoreduction of diluted CO₂: Metal-node-dependent activity and selectivity, *Angew. Chem. Int. Ed.* 57 (2018) 16811–16815.
- [24] K. Niu, Y. Xu, H. Wang, R. Ye, A spongy nickel-organic CO₂ reduction photocatalyst for nearly 100% selective CO production, *Sci. Adv.* 3 (2017) 1700921–1700929.
- [25] L. Yang, G. Zhu, H. Wen, X. Guan, X. Sun, H. Feng, W. Tian, D. Zheng, X. Cheng, Y. Yao, Constructing a highly oriented layered MOF nanoarray from a layered double hydroxide for efficient and long-lasting alkaline water oxidation electrocatalysis, *J. Mater. Chem. A* 7 (2019) 8771–8776.
- [26] B. Wang, J. Shang, C. Guo, J. Zhang, F. Zhu, A. Han, J. Liu, A general method to ultrathin bimetal-mof nanosheets arrays via in situ transformation of layered double hydroxides arrays, *Small* 15 (2019) 1804761–1804767.
- [27] B. Wang, M. Zhao, L. Li, Y. Huang, X. Zhang, C. Guo, Z. Zhang, H. Cheng, W. Liu, J. Shang, J. Jin, X. Sun, J. Liu, H. Zhang, Ultra-thin metal-organic framework nanoribbons, *Nat. Sci. Rev.* 7 (2020) 46–52.
- [28] B. Wang, J. Jin, B. Ding, X. Han, A. Han, J. Liu, General approach to metal-organic framework nanosheets with controllable thickness by using metal hydroxides as precursors, *Front. Mater.* 7 (2020) 37–43.
- [29] S. Wang, C.M. McGuirk, A. d'Aquino, J.A. Mason, C.A. Mirkin, Metal-organic framework nanoparticles, *Adv. Mater.* 30 (2018) 1800202–1800215.
- [30] K. Song, X. Qiu, B. Han, S. Liang, Z. Lin, Efficient upcycling electroplating sludge and waste PET into Ni-MOF nanocrystals for the effective photoreduction of CO₂, *Environ. Sci. Nano* 8 (2021) 390–398.
- [31] X. Xuan, M. Qian, L. Pan, T. Lu, L. Han, H. Yu, L. Wan, Y. Niu, S. Gong, A longitudinally expanded Ni-based metal-organic framework with enhanced double nickel cation catalysis reaction channels for a non-enzymatic sweat glucose biosensor, *J. Mater. Chem. B* 8 (2020) 9094–9109.
- [32] R. Sibille, A. Mesbah, T. Mazet, B. Malaman, S. Capelli, M. François, Magnetic measurements and neutron diffraction study of the layered hybrid compounds Mn(C₈H₄O₄)(H₂O)₂ and Mn₂(OH)₂(C₈H₄O₄), *J. Solid State Chem.* 186 (2012) 134–141.
- [33] X. Liu, X. Lv, H. Lai, G. Peng, Z. Yi, J. Li, A simple Ni-based metal-organic framework as catalyst for dye-sensitized photocatalytic H₂ evolution from water reduction, *Photochem. Photobiol.* 96 (2020) 1169–1175.
- [34] L. Liu, Y. Hai, Y. Gong, A facile electrosynthesis of terephthalate (tp)-based metal-organic framework, Ni₃(OH)₂(H₂O)₂(tp)₂ with superior catalytic activity for hydrogen evolution reaction, *Eur. J. Inorg. Chem.* 2020 (2020) 4215–4224.
- [35] A. Carton, A. Mesbah, T. Mazet, F. Porcher, M. François, Ab initio crystal structure of nickel(II) hydroxy-terephthalate by synchrotron powder diffraction and magnetic study, *Solid State Sci.* 9 (2007) 465–471.
- [36] A. Mesbah, P. Rabu, R. Sibille, S. Lebegue, T. Mazet, B. Malaman, M. François, From hydrated Ni₃(OH)₂(C₈H₄O₄)₂(H₂O)₄ to anhydrous Ni₂(OH)₂(C₈H₄O₄): impact of structural transformations on magnetic properties, *Inorg. Chem.* 53 (2014) 872–881.
- [37] Y. Jiao, J. Pei, C. Yan, D. Chen, Y. Hu, G. Chen, Layered nickel metal-organic framework for high performance alkaline battery-supercapacitor hybrid devices, *J. Mater. Chem. A* 4 (2016) 13344–13351.
- [38] P. Thangasamy, S. Shanmuganathan, V. Subramanian, A NiCo-MOF nanosheet array based electrocatalyst for the oxygen evolution reaction, *Nanoscale Adv.* 2 (2020) 2073–2079.
- [39] P. Qi, Y. Gu, H. Sun, Y. Lian, X. Yuan, J. Hu, Z. Deng, H.-C. Yao, J. Guo, Y. Peng, Active nickel derived from coordination complex with weak inter/intra-molecular interactions for efficient hydrogen evolution via a tandem mechanism, *J. Catal.* 389 (2020) 29–37.
- [40] Q. Liu, L. Xie, X. Shi, G. Du, A.M. Asiri, Y. Luo, X. Sun, High-performance water oxidation electrocatalysis enabled by a Ni-MOF nanosheet array, *Inorg. Chem. Front.* 5 (2018) 1570–1574.
- [41] J. Xiang, J. Liu, J. Xu, S. Su, H. Tang, Y. Hu, M.E. Mostafa, K. Xu, Y. Wang, S. Hu, The fluorescence interference in Raman spectrum of raw coals and its application for evaluating coal property and combustion characteristics, *Proc. Combust. Inst.* 37 (2019) 3053–3060.
- [42] G. Hai, X. Jia, K. Zhang, X. Liu, Z. Wu, G. Wang, High-performance oxygen evolution catalyst using two-dimensional ultrathin metal-organic frameworks nanosheets, *Nano Energy* 44 (2018) 345–352.
- [43] P. Man, B. He, Q. Zhang, Z. Zhou, C. Li, Q. Li, L. Wei, Y. Yao, A one-dimensional channel self-standing MOF cathode for ultrahigh-energy-density flexible Ni–Zn batteries, *J. Mater. Chem. A* 7 (2019) 27217–27224.
- [44] S.-M. You, W.M.A. El Roubi, L. Assaud, R.-A. Doong, P. Millet, Water photo-electrooxidation using mats of TiO₂ nanorods, surface sensitized by a metal-organic framework of nickel and 1,2-benzene dicarboxylic acid, *Hydrogen* 2 (2021) 58–75.
- [45] S. Liang, X. Zhong, Z. Zhong, B. Han, W. Chen, K. Song, H. Deng, Z. Lin, Biomimetic inspired porphyrin-based nanoframes for highly efficient photocatalytic CO₂ reduction, *Chem. Eng. J.* 411 (2021) 128414–128425.
- [46] B. Han, X. Ou, Z. Zhong, S. Liang, H. Deng, Z. Lin, Rational design of FeNi bimetal modified covalent organic frameworks for photoconversion of anthropogenic CO₂ into widely tunable syngas, *Small* 16 (2020) 2002985–2002991.
- [47] W. Chen, B. Han, C. Tian, X. Liu, S. Liang, H. Deng, Z. Lin, MOFs-derived ultrathin holey Co₃O₄ nanosheets for enhanced visible light CO₂ reduction, *Appl. Catal. B* 244 (2019) 996–1003.
- [48] S. Wang, B.Y. Guan, X.W. Lou, Rationally designed hierarchical N-doped carbon@NiCo₂O₄ double-shelled nanoboxes for enhanced visible light CO₂ reduction, *Energy Environ. Sci.* 11 (2018) 306–310.
- [49] W. Chen, X. Liu, B. Han, S. Liang, H. Deng, Z. Lin, Boosted photoreduction of diluted CO₂ through oxygen vacancy engineering in NiO nanoplatelets, *Nano Res.* 14 (2020) 730–737.
- [50] S. Liang, B. Han, X. Ou, X. Ye, W. Chen, H. Deng, C. Tian, Z. Lin, Lattice-strained nickel hydroxide nanosheets for the boosted diluted CO₂ photoreduction, *Environ. Sci. Nano* 8 (2021) 2360–2371.
- [51] P. Varadhan, H.-C. Fu, D. Priante, J.R.D. Retamal, C. Zhao, M. Ebaid, T.K. Ng, I. Ajia, S. Mitra, I.S. Roqan, B.S. Ooi, J.-H. He, Surface passivation of GaN nanowires for enhanced photoelectrochemical water-splitting, *Nano Lett.* 17 (2017) 1520–1528.
- [52] M. Ebaid, D. Priante, G. Liu, C. Zhao, M. Sharizal Alias, U. Buttner, T. Khee Ng, T. Taylor Isimjan, H. Idriss, B.S. Ooi, Unbiased photocatalytic hydrogen generation from pure water on stable Ir-treated In_{0.33}Ga_{0.67}N nanorods, *Nano Energy* 37 (2017) 158–167.
- [53] S. Liang, X. Liu, Z. Zhong, B. Han, X. Zhong, W. Chen, K. Song, H. Deng, Z. Lin, Lattice-strained nanotubes facilitate efficient natural sunlight-driven CO₂ photoreduction, *Nano Res.* 14 (8) (2021) 2558–2567.
- [54] W. Chen, B. Han, Y. Xie, S. Liang, H. Deng, Z. Lin, Ultrathin Co-Co LDHs nanosheets assembled vertically on MXene: 3D nanoarrays for boosted visible-light-driven CO₂ reduction, *Chem. Eng. J.* 391 (2020) 123519–123526.
- [55] B. Han, J. Song, S. Liang, W. Chen, H. Deng, X. Ou, Y.-J. Xu, Z. Lin, Hierarchical NiCo₂O₄ hollow nanocages for photoreduction of diluted CO₂: adsorption and active sites engineering, *Appl. Catal. B* 260 (2020) 118208–118214.
- [56] S. Wang, B.Y. Guan, X.W.D. Lou, Construction of ZnIn₂S₄-In₂O₃ hierarchical tubular heterostructures for efficient CO₂ photoreduction, *J. Am. Chem. Soc.* 140 (2018) 5037–5040.